THE ASTROPHYSICAL JOURNAL, 421:92–100, 1994 January 20

NEAR-INFRARED SPECTROSCOPIC IMAGING OF THE CIRCUMNUCLEAR ENVIRONMENT OF NGC 1068

M. BLIETZ, M. CAMERON, S. DRAPATZ, R. GENZEL, A. KRABBE, AND P. VAN DER WERF
Max-Planck-Institut für extraterrestrische Physik, Giessenbachstraße, Postfach 1603, D-85740 Garching bei München, Germany

A. STERNBERG
School of Physics and Astronomy, Tel Aviv University, Ramat Aviv, 69978, Israel

AND

M. WARD
Department of Physics, Nuclear Physics Laboratory, Keble Road, Oxford OX1 3RH, United Kingdom
Received 1993 February 22; accepted 1993 July 27

ABSTRACT

We report $\leq 1''$ resolution imaging of the 1.6435 μm [Fe II] and 2.1212 μm H_2 $v = 1$–0 $S(1)$ lines toward the nucleus of the Seyfert 2 galaxy NGC 1068. Our observations suggest that the near-infrared [Fe II] and H_2 emission, as well as the radio continuum and optical line emission observed toward the narrow-line region (NLR), arises at the interface between the nuclear outflow/radiation and dense ($n(H_2) > 10^4$ cm^{-3}) circumnuclear molecular clouds. The [Fe II] emission extends over $\geq 8''$, is elongated along P.A. $\sim 35°$ and tracks the NLR and the central collimated part of the twin radio jet. The [Fe II] emission may be produced in gas exposed to nuclear X-ray radiation or in gas which is interacting with the outflow/jet from the active nucleus. We also find that the abundance of iron appears to be enhanced along the jet axis. We propose that this enhancement may be due to efficient grain destruction by the hard nuclear radiation or fast J-shocks produced in the outflow and/or due to an unusually high value of the total fractional abundance of iron compared to solar. When leaving the molecular disk, the outflow/jet enters less dense atomic gas at a much lower pressure which causes the jet to widen, seen both in the [Fe II] and radio emission. Alternatively, and less likely, the [Fe II] emission may be emitted in gas shocked by supernova remnants. In contrast, the H_2 emission is concentrated at the nucleus and extends $\sim 5''$ (340 pc) east-west, with several embedded knots which probably represent concentrations of dense, massive molecular clouds. The high signal-to-noise quality of these new data have enabled us to ascertain that the warm molecular gas is not symmetrically distributed about the near-infrared continuum peak as was previously suspected. Rather, the brightest H_2 knot is centered $0''.2 \pm 0''.3$ southwest of the near-infrared continuum peak and, due to a total molecular hydrogen column density likely exceeding 10^{23} cm^{-2}, may contribute significantly to the obscuration of the broad-line region in the nucleus of NGC 1068.

Subject headings: galaxies: active — galaxies: individual (NGC 1068) — galaxies: ISM — galaxies: nuclei — galaxies: Seyfert — infrared: galaxies

1. INTRODUCTION

The bright and nearby ($d = 14$ Mpc, $1'' = 68$ pc for $H_0 = 75$ km s^{-1} Mpc^{-1}) Seyfert 2 galaxy NGC 1068 is one of the best-studied active galaxies. Optical imaging spectroscopy (Pogge 1988; Evans et al. 1991) has revealed a conical NLR containing clouds with complex gas motions (Walker 1968; Cecil, Bland, & Tully 1990). A bipolar synchrotron radio jet, $13''$ in extent and centered on the nucleus, is oriented along the NLR cone (Wilson & Ulvestad 1987). Broadline optical emission is visible in polarized light which is probably scattered and reflected from clouds which are directly exposed to radiation from an obscured Seyfert 1 type active galactic nucleus (AGN) (Antonucci & Miller 1985; Miller, Goodrich, & Mathews 1991).

Recently, Rotaciuc et al. (1991) presented the first spatially resolved ($\sim 1''.3$ FWHM) images of the nuclear 2.12 μm H_2 $v = 1$–0 $S(1)$ line emission region in NGC 1068. These observations, together with high-resolution ($\sim 3''$) interferometry measurements of the CO $J = 1$–0 rotational line emission at 2.6 mm (Planesas, Scoville, & Myers 1991) reveal a $\sim 5''$ diameter concentration of molecular gas, with an estimated mass of $\sim 3 \times 10^7$ $M_\odot$, in the immediate vicinity of the optical NLR. Rotaciuc et al. (1991) argue that most of the nuclear H_2 line emission is produced in clouds which are heated by UV or X-ray photons emitted by the obscured AGN.

Fe II line emission is a prominent feature of the optical and ultraviolet spectra of AGNs (Wills, Netzer, & Wills 1985), and in NGC 1068 both narrow forbidden and broad permitted Fe II emission lines have been detected (Snijders, Netzer, & Boksenberg 1986; Halpern & Oke 1986). A more useful tool for probing deep into the nuclei of active galaxies are the near-infrared [Fe II] line observations which benefit greatly from the much reduced extinction in this wavelength regime ($A_K \sim 1/12$ A_V). Near-infrared 1.6435 μm $^4D_{7/2}$–$^4F_{9/2}$ and 1.257 μm $^4D_{7/2}$–$^6D_{9/2}$ [Fe II] line emission has been detected in several Seyfert galaxies, including NGC 1068 (Oliva & Moorwood 1990; Mouri, Kawara, & Taniguchi 1993). Although these studies only marginally spatially resolved the [Fe II] emission-line region in NGC 1068, Oliva & Moorwood (1990) suggested that the emission is produced in gas shocked by an AGN wind or outflow.

In this paper we present the first high spatial resolution (FWHM $\sim 1''$) image of the [Fe II] 1.64 μm line emission and new high-resolution infrared imaging observations of the

2.12 μm $v = 1$–0 $S(1)$ vibrational molecular hydrogen (H_2) line emission from the nucleus of NGC 1068. These data reveal, for the first time, the detailed distribution of the 1.64 μm [Fe II] line emission in the nucleus of NGC 1068 and provide information on the excitation state and gas-phase abundance of iron in the nuclear environment, as well as on the interaction of the nuclear outflow/radiation with circumnuclear molecular clouds. In addition, our new H_2 observations provide an improved picture of the distribution and dynamics of molecular gas close to the NLR of NGC 1068.

2. OBSERVATIONS

The measurements reported here were made in 1991 July with the MPE $1 \rightarrow 5$ μm imaging spectrometer, FAST (Rotaciuc 1992), at the 4.2 m William Herschel Telescope (WHT) in La Palma, Canary Islands. FAST uses a 58×62 pixel InSb array detector manufactured by Santa Barbara Research Center in tandem with a circular variable filter (CVF) and a Queensgate scanning Fabry-Pérot spectrometer, resulting in a resolving power of 950 for the observations of the 2.12 μm $v = 1$–0 $S(1)$ line of H_2. For the observations of the 1.64 μm [Fe II] line we used the CVF only which has a spectral resolving power of 55. The pixel scale was 0.″5 which, together with the $\leq 1''$ optical seeing at the time of our observations, resulted in a spatial resolution of our line images of 0.″8–1.″0 FWHM.

The data were reduced using the MIDAS package. In the case of the $S(1)$ line of H_2, we took line images at 890, 1100, and 1315 km s^{-1} with an exposure time of 200 s each. Several sets of such 200 s integration data were taken, but for the present analysis only the data obtained under best seeing conditions ($< 1''$) were selected. After subtraction of the dark current, the individual source and sky frames were flat-fielded, differenced, and hot pixels were interpolated. The resulting line-plus-continuum images were rebinned unto a grid of 0.″025 pixels and recentered on the continuum peak of NGC 1068. Using standard star measurements the line-plus-continuum images were corrected for atmospheric transmission and the instrumental profile. Finally, the mean of the continuum on either side of the line was subtracted. The resulting line images were coadded, resulting in a line flux map with a total integration time of 1200 s. In order to low-bandpass filter the data to remove artifacts which arise from slight seeing variations, the Lucy-Richardson algorithm (Lucy 1974) was applied to each map and the images were subsequently convolved to their original spatial resolution.

In the case of [Fe II], images of integration time 50 s were taken on the line and on the adjacent continuum with a total integration time of 3200 s on the line. Great care has been taken to ensure accurate continuum subtraction since in low-resolution CVF mode the line to continuum ratio at the continuum peak of NGC 1068 is only $\sim 3\%$. Comparison of the two continua on either side of the line shows a mean rms spatial variation of $\leq 1\%$, which includes the intensity difference between the two continua, and is thus an estimate of the accuracy of our continuum subtraction. As such, details of the [Fe II] distribution within $\sim 1''$ of the continuum peak are dependent on the continuum subtraction. Regions further away ($> 1''$) from the continuum peak are less affected since the line to continuum ratio raises (up to $\sim 6\%$) with increasing distance from the nucleus. Subsequent data reduction steps were then identical to those applied to the H_2 data.

3. RESULTS AND DISCUSSION

3.1. *Spatial Distribution of* [Fe II] *and* H_2 *Line Emission*

Figure 1 shows the total line flux maps of the [Fe II] and H_2 lines at a spatial resolution of 1.″0 and 0.″8, respectively. The

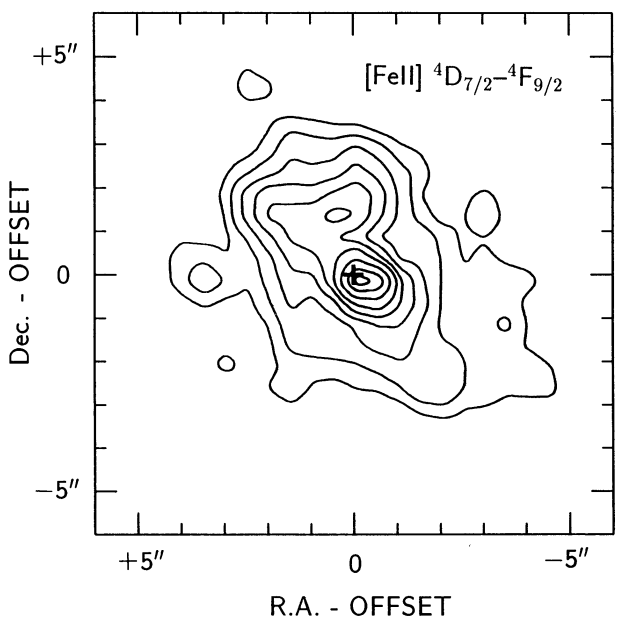

FIG. 1*a*

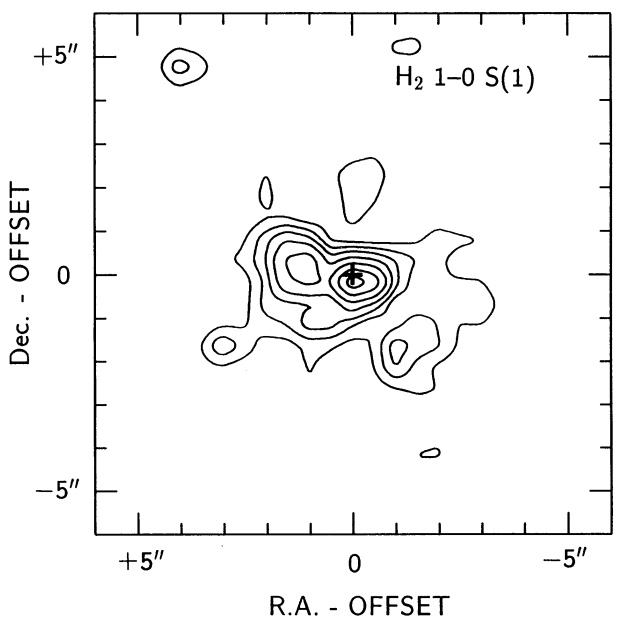

FIG. 1*b*

FIG. 1.—(*a*) 1.″0 resolution map of the [Fe II] $^4D_{7/2}$–$^4F_{9/2}$ transition at 1.6435 μm. Contour levels are 7%, 10%, 16%, 24%, 33%, 43%, 59%, 79%, and 95% of the peak surface brightness which is 2.3×10^{-3} ergs cm^{-2} s^{-1} sr^{-1}. The lowest contour level corresponds to 2 σ. (*b*) 0.″8 resolution map of the H_2 $v = 1$–0 $S(1)$ line at 2.1212 μm integrated over the velocity range 890–1315 km s^{-1}. Contour levels are 10%, 17%, 24%, 33%, 47%, 67%, and 91% of the peak surface brightness which is 2.1×10^{-3} ergs cm^{-2} s^{-1} sr^{-1}. The lowest contour level corresponds to 3 σ. The crosses in (*a*) and (*b*) mark the near-infrared continuum peak.

TABLE 1

[Fe II] 1.64 μm AND H_2 2.12 μm SURFACE BRIGHTNESSES[a] FOR INDIVIDUAL FEATURES AND TOTAL LINE FLUXES[b]

Feature/Line	H_2 2.12 μm	[Fe II] 1.64 μm
Nucleus	4.0×10^{-3}	2.0×10^{-3}
Eastern knot	5.4×10^{-4}	...
Flare peak	...	9.8×10^{-4}
Total flux	14×10^{-14}	26×10^{-14}

NOTE.—The surface brightnesses of the [Fe II] and H_2 line are a mean over 1".0 and 0".8, respectively.

[a] In ergs cm^{-2} s^{-2} sr^{-1}.

[b] In ergs cm^{-2} s^{-1}.

total line fluxes and mean surface brightnesses of individual features in these maps are listed in Table 1. In addition, Figure 2 shows overlays of the [Fe II] and H_2 emission on the 0".4 resolution 5 GHz radio continuum map of Wilson & Ulvestad (1983). The overlays have been aligned with our total line flux maps as following: the absolute position of the 2 μm continuum peak (R.A. = $02^h40^m07^s.08$, Decl. = $-00°13'31".5 \pm 1"$ [1950]; Scoville et al. 1988; Thronson et al. 1989) is not sufficiently well determined to align the near-infrared line emission maps at subarcsecond accuracy with images obtained at other wavelengths. We therefore assume that the near-infrared and optical (Lynds 1991) continuum peaks are spatially coincident, consistent with recent adaptive optics observations (Gallais 1991), which show that any offset between *J*/*H*/*K*-band peaks and the central compact source in the visible is less than ~0".4. We then use the relative positions of the radio to optical emission determined by Evans et al. (1991). Evans et al. (1991) identify the three prominent central peaks in the high-resolution 15 GHz map of Ulvestad, Neff, & Wilson (1987) with three [O III] peaks so that an alignment of radio and optical coordinates at subarcsecond accuracy becomes possible.

The distribution of the 1.64 μm [Fe II] emission, shown in Figure 1*a*, is extended over 8" × 4" along P.A. 30 to 40° east of north. There is a compact line emission peak centered 0".3 southwest of the continuum centroid, as well as a more extended structure that is brightest 1".5 northeast of the near-infrared nucleus. However, due to the relatively low line to continuum ratio (~3%) at the continuum peak, the positional offset between the line and continuum centroids cannot be realistically determined to an accuracy better than ~0".3. Therefore the radial offset between line and continuum centroids is 0".3 ± 0".3. When account is taken of the different angular resolution of the two maps overlaid in Figure 2*a*, the *brighter* [Fe II] emission appears well spatially correlated with the 5 GHz bipolar radio jet that traces the fast outflow from the nucleus. The [Fe II] emission decreases rapidly in brightness where the radio jet appears to flare (that is, to increase its width perpendicular to the jet axis) at ~2"–3" northeast of the nucleus. This suggests that the [Fe II] emission traces the radio jet because an interaction between either the nuclear outflow or the hard nuclear radiation and the circumnuclear gas creates large columns of Fe^+ ions. In addition, Figure 2*a* shows at low contour levels faint structure that extends on both sides of the jet over a region almost as long as the jet. This emission could originate in gas exposed to the nuclear radiation due to a relatively extinction-free view of the AGN. In contrast, the *brighter* [Fe II] emission seems to be gas at the *interface* of the NLR cone, exposed to the hard nuclear radiation which escapes along the possibly near–extinction-free outflow/cavity. This would be the case if the molecular material in the vicinity of the NLR is in the form of clumpy giant molecular clouds, as indicated for the NLR by the *HST* [O III] measurements (Evans et al. 1991; see also Cameron et al. 1993). In this scenario, certain lines of sight to the narrow line clouds would encounter extremely high attenuation while others would offer a relatively extinction-free view.

The overall distribution of the H_2 emission (see Fig. 1*b*) not only shows a prominent maximum close to the 2 μm continuum peak but also reveals an extended structure 5" in size with several embedded knots, in agreement with the observation of Rotaciuc et al. (1991). Our new data also reveal faint extended emission further away from the nucleus. As in the case of the [Fe II] emission, this faint emission component is likely due to gas which does not have an extinction-free view of the active nucleus. A fainter H_2 peak 2" north of the continuum maximum is present on both the 1100 and 1315 km s^{-1} maps. At our velocity resolution of 315 km s^{-1} it is apparent that the individual emission knots have radial velocities differing by up to 250 km s^{-1}: the central, southwestern and eastern knots are centered at ~1080, 1150, and 1250 km s^{-1} respectively. This is indicative of large-scale streaming of molecular gas but is not necessarily consistent with a simple rotation pattern. The ~2" east-west separation between the two brightest knots and the finding that the eastern knot is at higher velocity than the western knot is also in good agreement with Rotaciuc et al. (1991). Our higher spatial resolution data show that these two knots are *not* distributed symmetrically about the continuum peak, as found by Rotaciuc et al. (1991), but that the brightest emission knot coincides (within the positional uncertainty) with the continuum peak: the 2.12 μm centroid of the brightest H_2 knot (see Fig. 1*b*) is ~0".2 south and 0".1 west of the 2 μm continuum centroid which corresponds to a radial offset of ~0".2. Again, due to the low line to continuum ratio (~3%) at the continuum peak, the positional offset between the line and continuum centroids cannot be realistically determined to an accuracy better than ~0".3. Therefore the radial offset between line and continuum centroids is 0".2 ± 0".3. In summary, we conclude that the peaks of the [Fe II] and the H_2 emission are coincident within the positional uncertainty (and are, within the errors, also coincident with the 1.6–2.1 μm continuum peak), if one assumes that the maxima of the continuum emission at 1.6 and 2.1 μm fall on top of one another.

3.2. H_2 *Emission, Nuclear Outflow, and Obscuration*

The radio jet is brightest and best collimated *within* the east-west extended H_2 emission region. Just *outside* the H_2 region the radio emission northeast and southwest of the nucleus appears to flare. The most intense part of the radio jet northeast of the nucleus is bordered by H_2 knots to the north and to the east, as is one of the two bright radio peaks southeast of the nucleus. Our observations thus suggest a close physical connection between circumnuclear molecular clouds, radio jet and the related nuclear outflow. The outflow may have cleared a channel of molecular material which in turn is surrounded by dense molecular clouds. Alternatively, an initially isotropic outflow from the nucleus may have been channeled into the observed bipolar structure by the circumnuclear molecular clouds. A clear-cut decision on the origin of the confining agent from our observations is currently not possible. However, we emphasize that the double-lobed structure seen in the H_2

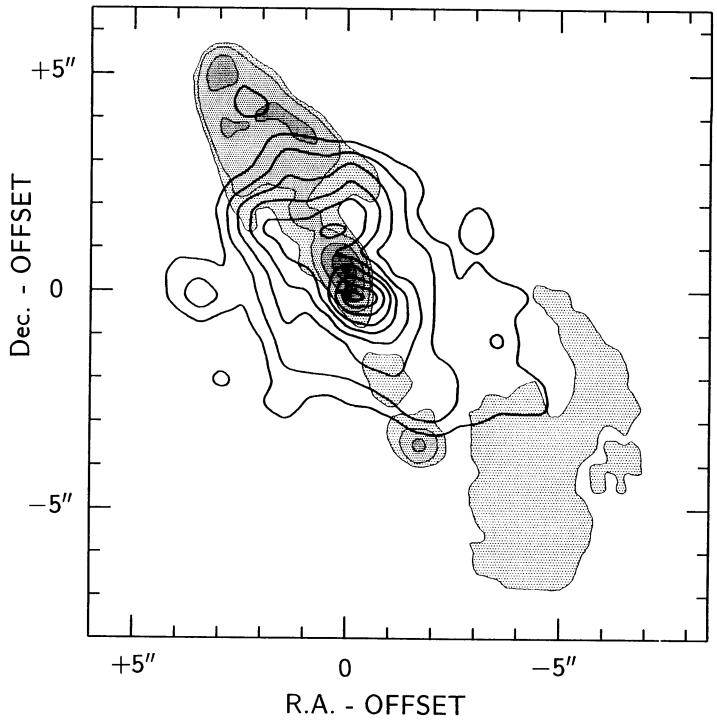

FIG. 2a

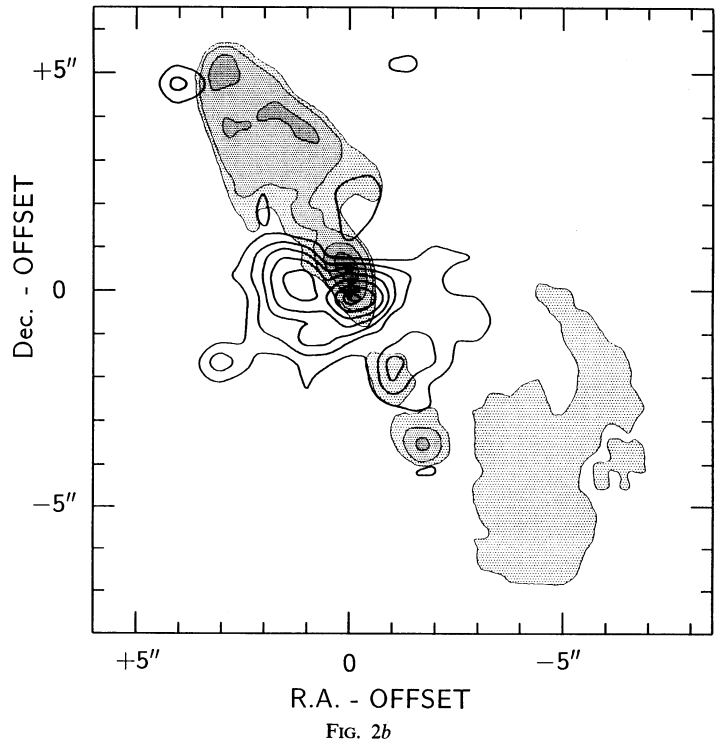

FIG. 2b

FIG. 2.—Overlay of the 5 GHz radio continuum map (*shaded*) of Wilson & Ulvestad (1983, 0.″4 resolution) on (*a*) the [Fe II] emission of Fig. 1*a* and (*b*) on the H_2 emission of Fig. 1*b*.

image (see Fig. 1*b*) seems not to form a confining torus. This is suggested by the fact that the two knots seen at the nucleus and 2″ to the east are not distributed symmetrically about the continuum peak and that the velocity channels of the 250 km s^{-1} velocity spread H_2 emission do not show a simple rotational pattern in our 300 km s^{-1} resolution data.

Averaged over the central 0.″8 (50 pc) the H_2 flux (4.8×10^{-14} ergs cm^{-2} s^{-1}; see Table 1) of the central, unresolved H_2 knot just southwest of the nucleus corresponds to a column density of 10^{19} cm^{-2} and warm molecular hydrogen mass of 600 $M_\odot$ if a thermal population at 2000 K is assumed (Rotaciuc et al. 1991). This requires molecular hydrogen vol-

ume densities in excess of 5×10^4 cm^{-3}, the critical density of the $v = 1$ state (Sternberg & Dalgarno 1989). The total molecular mass in the central 3″ may be estimated from the intensity of the 115 GHz CO line emission measured by Planesas et al. (1991), and it follows that the ratio of hot to total H_2 gas in the nucleus is probably between 10^{-4} and 10^{-5}. The implied average total molecular hydrogen column density in the central 50 pc is 10^{23} to 10^{24} cm^{-2}. Even when neglecting extinction within the H_2 source itself, these large H_2 column densities correspond to visual extinctions ranging from $A_V = 50^m$ to 500^m (assuming a dust to gas ratio of 10^{-2}). This estimate is in agreement with the visual extinction derived from the mid-IR dust emission (Cameron et al. 1993). It therefore appears plausible that the central H_2 knot contributes significantly to the large obscuration of the nucleus that has been inferred by Antonucci & Miller (1985) from optical polarization observations. However, as discussed by Cameron et al. (1993), we emphasize that the H_2 knot coincident with the nucleus *cannot* represent the parsec-scale dusty torus proposed by Antonucci & Miller (1985), since this structure would not allow radiation to escape at angles $\geq 30°$ beyond the outflow and excite molecular gas lying in that direction. This is contrary to the observed morphology of the H_2 distribution.

3.3. *Origin of the* [Fe II] *Emission*

3.3.1. *Basic Equations*

The 1.6435 μm [Fe II] $^4D_{7/2}$–$^4F_{9/2}$ forbidden emission line has been observed in several starburst and Seyfert galaxies (Oliva & Moorwood 1990; Mouri et al. 1993). In the Milky Way infrared [Fe II] line emission has been observed in H II regions (Lowe, Moorhead, & Welhau 1979), supernova remnants (Graham, Wright, & Longmore 1987; Oliva, Moorwood, & Danziger 1989) and the Galactic center (De Poy 1992). In combination with other near-infrared lines which similarly trace warm gas, in particular the Brγ line at 2.165 μm, this [Fe II] line has proved to be a powerful tool in attempts to discriminate between the various excitation mechanisms active in such regions. Here we focus on the use of the spatially resolved [Fe II]/Brγ ratio as a diagnostic of the physical conditions prevailing in the inner few hundred parsec of NGC 1068. We first derive an analytical approximation for the intensity of the [Fe II] line emission and proceed to calculate the theoretical [Fe II]/Brγ ratio as a function of temperature, density, and abundance.

The $a\,^4D_{7/2}$ level of Fe^+ lies 1 eV (12,000 K) above the ground state so that the 1.64 μm line is produced by electron impact excitation in hot ($\sim 10^4$ K) ionized gas in many astrophysical sources. The radiative lifetime of the $a\,^4D_{7/2}$ level is 78 s (Nussbaumer & Storey 1988) and the critical electron density at which the rates of radiative and collisional deexcitation of the transition are equal is $\sim 4.2 \times 10^4 T_4^{0.69}$ cm^{-3}, where T_4 is the gas temperature in units of 10^4 K. In order *to estimate the intensity* of collisionally excited [Fe II] 1.64 μm line emission for a variety of cloud conditions we have, for a wide range of electron densities and gas temperatures, numerically solved the equations of detailed balance for the equilibrium level populations of a 16 level system which includes all of the fine-structure levels of the lowest four terms ($a\,^6D$, $a\,^4F$, $a\,^4D$, and $a\,^4P$) of the Fe^+ ion. We assumed that the levels are populated by electron impact excitations and deexcitations and (optically thin) radiative transitions. We used the level energies measured by Johansson (1978) and the radiative transition probabilities computed by Nussbaumer & Storey (1988) and adopted the new electron collision strengths computed by Pradhan & Zhang (1993). These collision strengths are probably more accurate than those given by Nussbaumer & Storey (1980) due to the use of a 38 state close coupling expansion. Figure 3 shows the result of our numerical calculations. The symbols indicate the computed intensities of the [Fe II] 1.64 μm line for several electron densities and gas temperatures and an assumed Fe^+ column density of 10^{16} cm^{-2}. The effects of internal or foreground extinction have been neglected.

In order to approximate our numerical results analytically, we have carried out least-square fits to the numerical data points using a fit function of the form

$$I(n_e, T) = \frac{T_4^{-0.94} e^{-1.57/T_4} (N_{Fe^+}/10^{16})}{(1 + 4.2 \times 10^4 T_4^{0.69}/n_e)}, \quad (1)$$

where n_e is the electron density (in units of cm^{-3}) and N_{Fe^+} is the Fe^+ column density (in units of cm^{-2}). This expression gives the line intensity for an *effective two-level system* consisting of the Fe^+ ground $a\,^6D_{9/2}$ state and the upper and lower levels of the $a\,^4D_{7/2}$–$a\,^4F_{9/2}$ 1.6435 μm transition. From Figure 3 it is obvious that this analytical approximation follows reasonable well the numerical data points for temperatures greater than $\sim 10^3$ K and densities higher than 10^4 cm^{-3}. We will restrict use of our fit to this parameter space which, as will be argued in § 3.3.2, is also a realistic assumption for the NLR in NGC 1068.

We can rewrite equation (1) in a more general form by substituting $N_{Fe^+} = \delta X_{Fe\odot}(N_H + N_{H^+}) f_{II}$ where δ denotes the gas phase iron abundance relative to the total fractional abundance of iron (which we will for simplicity refer to in the following as the "gas phase iron abundance"), $X_{Fe\odot}$ is the solar abundance of iron relative to hydrogen, $(N_H + N_{H^+})$ is the

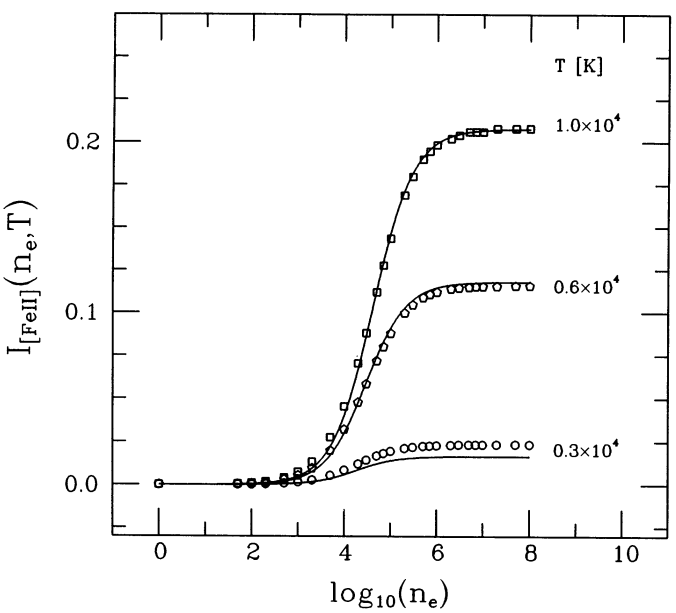

FIG. 3.—Calculated surface brightness (ergs cm^{-2} s^{-1} sr^{-1}) of the 1.6435 μm [Fe II] $^4D_{7/2}$–$^4F_{9/2}$ line emission for an assumed Fe^+ column density of $N_{Fe^+} = 10^{16}$ cm^{-2} for various electron densities (cm^{-3}) and temperatures. The symbols represent the numerically calculated intensities for selected temperatures while the solid lines represent least-square fits to an effective two-level approximation.

total column density of hydrogen nuclei in the Fe^+ zone, and f_{II} is the average fraction of singly ionized iron in the gas phase relative to total iron in the gas phase. We correct for extinction using the average Galactic interstellar extinction law of Savage & Mathis (1979), which, in the range $0.4 < \lambda[\mu m] < 3.4$, is given by $A_\lambda/E(B-V) = 1.313\lambda^{-1.41}$ (Greenhouse et al. 1991). Use of the Galactic interstellar extinction law is consistent with recent studies of Laor & Draine (1993), who find that the grain properties in the vicinity of the active nucleus may be similar to those in the Galaxy.

Taking the ratio between visual extinction A_V (see § 3.3.2) and color excess $E(B-V)$ as given by Schultz & Wiemer [1975; $A_V/E(B-V) = 3.14$] and the solar abundance of iron as given by Morton (1991: $X_{Fe_\odot} = 3.2 \times 10^{-5}$), the [Fe II] line intensity (ergs cm^{-2} s^{-1} sr^{-1}) can be written in the specific form

$$I_{[FeII]} = 3.2 \times 10^{-21} \frac{e^{-0.19A_V} T_4^{-0.94} e^{-1.57/T_4} (N_H + N_{H^+}) \delta f_{II}}{(1 + 4.2 \times 10^4 T_4^{0.69}/n_e)} . \quad (2)$$

We now calculate the intensity ratio of [Fe II] 1.64 μm and 2.1655 μm $n = 7$–4 Brγ hydrogen recombination line emission. Use of this ratio as diagnostic is justified if we *assume* that both the [Fe II] and the Brγ emission come from the same regions. This is likely to be the case if the near-infrared emission originates in the interface zones between circumnuclear molecular clouds and nuclear outflow/radiation as suggested by our observations. Such a tight correlation between these two emitting regions is also suggested by the morphology of the [Fe II] in Figure 1*a* and that of the Brγ in Figure 1 of Rotaciuc et al. (1991), although part of the [Fe II] emission is also extended beyond the interface region. Using the Brγ line intensity for case B recombination (Osterbrock 1989), the ratio, R, of the [Fe II] to Brγ intensity from a body of arguments, including the reddening term, then becomes

$$R = \frac{10^2 e^{-0.06A_V} T_4^{0.07} e^{-1.57/T_4} \delta(f_{II}/\xi)}{(1 + 4.2 \times 10^4 T_4^{0.69}/n_e)} , \quad (3)$$

where $\xi = n_e/(n_H + n_{H^+})$ denotes the average ionized fraction in the Fe^+ zone. This expression is independent of the total hydrogen column density.

Equation (3), together with the observed Brγ and [Fe II] line strengths, observationally derived values for the electron density, gas temperature, and extinction can be used to determine the gas phase iron abundance δ. Knowledge of δ provides, by itself, important information on the underlying physical processes as will be shown in § 3.3.3. Having obtained a value for the gas phase iron abundance δ, we can then proceed to use equation (2) to estimate the hydrogen column density of the emitting gas.

3.3.2. *Observed Parameters in the Nucleus of NGC 1068*

In this section we list our measured [Fe II] to Brγ ratios and derive estimates from observational results of the physical parameters electron density, gas temperature, and excitation, which are required inputs of equations (2) and (3).

I. Measured [Fe II] to Brγ ratios

A. *Nucleus.*—Our [Fe II] map gives a surface brightness of 2×10^{-3} ergs cm^{-2} s^{-1} sr^{-1} for the inner 1″ (see Table 1). From the Brγ map of Rotaciuc et al. (1991) we get $I_{Br\gamma} = 8.1 \times 10^{-4}$ ergs cm^{-2} s^{-1} sr^{-1} in the nucleus. Thus $R = 2.5$. This ratio is also consistent with measurements of the [Fe II] 1.25 μm and Paβ lines carried out by Ward et al. (1987), which indicate a ratio of [Fe II] 1.25 μm to Paβ of ~ 0.7. Using Case B recombination theory and correcting for extinction, this ratio corresponds to $R = 2.1$. In our analysis we adopt a mean value of $R_{nucleus} = 2.3$.

B. *Flare region.*—From our [Fe II] map we measure a [Fe II] surface brightness of 9.8×10^{-4} ergs cm^{-2} s^{-1} sr^{-1} (see Table 1) at the position of the flare peak, which lies $\sim 1\farcs5$ northeast of the nucleus. Using the [N II] surface brightness and the [N II]/Hα-ratio measured by Cecil et al. (1990), the expected [Fe II] to Brγ ratio becomes $R = 4.1$. This result is also consistent with the ratio of [Fe II] 1.25 μm to Paβ of ~ 1.0, as measured by Ward et al. (1987) which corresponds to $R = 3.1$. We again adopt a mean value of $R_{flare} = 3.6$.

II. Derived Parameters for the NLR

A. *Density.*—Mean rms electron densities of 3×10^4 cm^{-3} and 10^5 cm^{-3} for the flare region and the nucleus, respectively, have been derived from [N II] optical line measurements by Cecil et al. (1990). These densities are consistent with the mean density of 1.5×10^4 cm^{-3} for the inner $\sim 4''$ as given by Koski (1978). It should be noted, however, that *if* the emission region is very clumpy, as indicated for the NLR by the *HST* [O III] measurements (Evans et al. 1991; see 3.1), the actual local electron densities might be larger, perhaps reaching a few 10^6 cm^{-3} in the NLR clouds. We will therefore also consider this high-density case in the discussion below.

B. *Temperature.*—The [Fe II] λ8617 to 1.64 μm line ratio can be used as a temperature diagnostic. Halpern & Oke (1986) measure an upper limit of 0.02 for the ratio of [Fe II]λ8617 to [S II] $\lambda\lambda$6717 + 6731. The [S II] flux has been measured by Koski (1978) in a $4\farcs0 \times 2\farcs7$ slit to be 2.35×10^{-12} ergs cm^{-2} s^{-1}. Integration of our [Fe II]1.64 μm map within Koski's slit gives a flux of 1.8×10^{-13} ergs cm^{-2} s^{-1}. Taking into account differential extinction ($A_V = 0\overset{m}{.}9$, see below) we get an upper limit for the ratio I[Fe II] λ8617/I[Fe II] 1.64 μm < 0.3. Nussbaumer & Storey (1988) calculated this ratio as a function of n_e and T. Using their result and our upper limit we derive an upper limit for the temperature: $T \leq 10^4$ K for $n_e > 10^4$ cm^{-3}.

C. *Extinction.*—Optical line measurements indicate a mean visual extinction in the inner few hundred parsecs of $A_V = 1\overset{m}{.}3$ (Cecil et al. 1990). A second method for determining the extinction involves use of the [Fe II] 1.257 μm $^4D_{7/2}$–$^6D_{9/2}$ to 1.64 μm line ratio. Since both lines arise from the same upper level (a $^4D_{7/2}$), this ratio is *in*dependent of density and temperature and is a good probe of differential extinction. Oliva & Moorwood (1990) measure a 1.25 μm to 1.64 μm ratio in a $6'' \times 6''$ aperture of 1.30, only slightly smaller than the theoretical zero extinction value of 1.36 (Nussbaumer & Storey 1988). Again adopting the Galactic interstellar extinction law of Savage & Mathis (1979), this implies a visual extinction of $A_V \sim 0\overset{m}{.}5$ which, given the uncertainties, is close to the optically derived value. In the following we will use the mean of optical and near-infrared derived extinctions $A_V = 0\overset{m}{.}9$.

Such low values of A_V are in apparent contradiction to those derived from the measured column density of H_2 (see § 3.2). However, these two measurements can be reconciled if the molecular material in the vicinity of the NLR is in the form of clumpy giant molecular clouds (GMCs). In this case, certain lines of sight to the narrow-line clouds would encounter extremely high attenuation while others would offer a relatively extinction-free view of the ionized clouds (see § 3.1).

3.3.3. *Cloud Conditions in the Circumnuclear Environment*

Before we determine the gas phase abundance of iron using equation (3), we need to estimate f_{II}/ξ, the ratio of the fraction of singly ionized iron to ionized hydrogen. Since f_{II} is always ≤ 1 and assuming that the ionized hydrogen fraction ξ is determined only by hydrogen photoionization and radiative recombination, we can derive the following upper limits for f_{II}/ξ under different prevailing cloud conditions:

1. H II *region–type cloud conditions.*—For an H II region type origin of the [Fe II] emission we will assume $f_{II}/\xi \leq 0.2$. As has already been demonstrated by Oliva et al. (1989) and Mouri et al. (1993), this low fraction of singly ionized iron to ionized hydrogen follows immediately from the less effective charge exchange recombination of higher ionized iron with neutral hydrogen in the thin H II–H I transition region.

2. *Photon-dominated regions (PDRs).*—"Standard" PDR models (Sternberg & Dalgarno 1989) predict $\xi = 10^{-4}$ so that $f_{II}/\xi \leq 10^4$.

3. *X-ray photoionized gas.*—Models for gas heated by X-rays from a nonthermal power-law source (Halpern & Grindlay 1980) predict $\xi \sim 0.5$ in the broad H II to H I transition region, so that $f_{II}/\xi \leq 2$.

However, due to harder X-rays penetrating deeper into the cloud, *extended* regions of X-ray photoionized gas with large neutral fractions may form so that $\xi \sim 10^{-2}$ and $f_{II}/\xi \leq 10^2$.

4. *J-shocks.*—Using models of radiative *J*-shocks (Shull & McKee 1979) we estimate $\xi \sim 0.5$ for shock velocities $v_s > 40$ km s^{-1}. Thus $f_{II}/\xi \leq 2$.

For these differing regimes we now estimate the gas phase iron abundance δ for different cloud conditions using equation (3) as a means to differentiate between the possible mechanisms giving rise to the [Fe II] emission. In addition we also calculate the inferred hydrogen column densities using equation (2).

1. H II *region type.*—Our measured [Fe II]/Brγ ratios would require gas phase iron abundances of $\delta > 100\%$. H II regions are therefore effectively excluded.

2. *PDRs.*—In "normal" PDRs (Sternberg & Dalgarno 1989) the temperature is $T \leq 2 \times 10^3$ K. As a consequence the [Fe II] intensity is very low, requiring unphysically high abundances ($\delta \gg 100\%$) to account for our observed [Fe II]/Brγ ratio. Standard PDRs can therefore be firmly excluded.

3. *X-ray-photoionized gas.*—For "standard" X-ray models (Halpern & Grindlay 1980) we calculate $\delta_{\rm nucleus} \geq 15\%$ and $\delta_{\rm flare} \geq 20\%$. In the high-density case ($n_e \geq 10^6$ cm^{-3}) we obtain smaller values for δ: $\delta_{\rm nucleus} \geq 6\%$ and $\delta_{\rm flare} \geq 9\%$. The required hydrogen column densities are, in both density regimes, $N \sim 2$–4×10^{19} cm^{-2}.

In the case of *extended* regions of X-ray photoionized gas the temperature is likely to be $T \sim 3000$ K. For both density regimes we then obtain $\delta_{\rm nucleus} \geq 5\%$–$6\%$ and $\delta_{\rm flare} \geq 8\%$–$12\%$. We infer hydrogen column densities (both density regimes) of $N \sim 3$–9×10^{20} cm^{-2}.

4. *J-shocks.*–For *J*-shocks we calculate $\delta_{\rm nucleus} \geq 15\%$ and $\delta_{\rm flare} \geq 20\%$, whereas we obtain $\delta_{\rm nucleus} \geq 6\%$ and $\delta_{\rm flare} \geq 9\%$ in the high-density case. The hydrogen column densities are $N \sim 2$–4×10^{19} cm^{-2}.

The results of our calculations in 1–4 can be summarized as following:

1. Possible origins for the [Fe II] emission are either X-ray ionized gas or gas behind fast *J*-shocks (or a mixture of both), requiring hydrogen column densities ranging from 2×10^{19} up to 9×10^{20} cm^{-2}.

2. The gas phase iron abundance seems to be enhanced compared to the galactic value of 2% (Steenberg & Shull 1988) by factors ranging between ~ 2 and 10. A possible explanation in the case of X-ray ionized gas is the destruction of dust grains by the intense nuclear radiation field, releasing large amounts of grain-bound iron into the gas phase. In the case of *J*-shocks the required high values for the gas phase iron abundance could find a natural explanation in the dust-destroying capabilities of shocks faster than 40 km^{-1}; Seab & Shull (1983) have calculated the gas phase iron abundance in the cooling postshock zones of 40–120 km s^{-1} fast *J*-shocks and predict $\delta = 15\%$–60% in good agreement with our derived values. We note that a comparison with published shock models is justified since the hydrogen column densities predicted by the shock models are in good agreement with the ones required by our measurements: Taking the above derived lower limits for the gas phase iron abundances and an upper limit of $\delta \leq 60\%$ which is the maximum value given by published shock models (e.g., Seab & Shull 1983), we find using equation (2) that the hydrogen column densities required to reproduce our observed [Fe II] intensities would have to be 1–4 $\times 10^{19}$ cm^{-2} for the nucleus and 1–2 $\times 10^{19}$ cm^{-2} for the flare region. These column densities agree with the theoretically predicted values for the postshock cooling zone (a few times 10^{19} cm^{-2}; see, e.g., Seab & Shull 1983; Shull & Draine 1987).

An alternative to an enhancement of the *gas phase* iron abundance is a higher value of the *total* fractional abundance of iron compared to solar, as suggested by Marshall et al. (1993) from modeling of X-ray emission line observations, or a mixture of both. We therefore conclude that our analysis provides evidence for an enhancement of the iron abundance, either compared to solar, in the gas phase or both.

3.3.4. *An AGN Origin for the* [Fe II] *Emission*

In the previous section we have shown that possible cloud conditions for the [Fe II] emitting region are either X-ray ionized gas or gas behind fast *J*-shocks or both. There is, however, still the open question of an AGN *or* stellar origin for the [Fe II]. In order to shed more light onto this question we point out that the observed morphology of the [Fe II], H_2, radio and optical emission provides considerable evidence for an AGN like origin of the [Fe II]: As has already been shown in §§ 3.1 and 3.2, our observations suggest that the *interface* between nuclear outflow/radiation and circumnuclear molecular clouds is an obvious choice for the zone of [Fe II] emission. In this case the [Fe II] emission could be produced in molecular clouds exposed to X-ray radiation from the active nucleus or in gas interacting with the outflow from the nucleus, or possibly as combination of both.

When comparing the distribution of the [Fe II], radio, and H_2 emission in more detail, the [Fe II] seems even closer related to the nuclear outflow as we will discuss in the following: outside a projected radius of $\sim 4''$ (270 pc) the radio continuum emission northeast and southwest of the nucleus seems to flare and then terminates in a bow-shaped lobe on either side (Wilson & Ulvestad 1983, 1987). Wilson & Ulvestad (1987) model these lobes as bow shocks where the jet head strikes the surrounding interstellar medium. As shown in §§ 3.1 and 3.2, the onset of flaring is spatially coincident with a sudden drop in H_2 and [Fe II] emission (see Fig. 2*a*), both of which originate in dense ($n(H_2) > 10^4$ cm^{-3}) gas. We thus propose that at this

radius the jet emerges from the dense molecular disk and enters lower density atomic gas that possesses a much larger scale height.

Cecil et al. (1990) conclude that the jet axis is inclined by $\sim 45°$ relative to the galactic plane of NGC 1068 so that with an inclination of that plane to the line of sight of $\sim 35°$ (0° is face on) a projected radius of 270 pc corresponds to a height above the plane of 190 pc. In our own Galactic center the z-scale height of molecular clouds is ~ 50 pc and there are a few clouds extending up to 3 times that height (Bally et al. 1988). Taking into account that in a perturbed system such as NGC 1068 molecular clouds may be located at higher z-height than in our Galaxy, a value of 190 pc for the upper boundary of the molecular cloud population in NGC 1068 does not seem implausible. It then follows that the bow shock is in a low-density atomic medium and that at 190 pc height there is a fairly sudden change of pressure in the interstellar medium. Assuming that the shock at the head of the jet advances at a velocity of v_s into a surrounding medium of density ρ_0 and that the off-axis pressure of the shocked jet material inside of the bow lobes is p_i, the standoff angle α between jet axis, and the leading edges of the bow shock is given by a simple ram pressure argument

$$\sin^2(\alpha) = p_i/(\rho_0 \times v_s^2) . \quad (4)$$

The radio maps of Wilson & Ulvestad (1983, 1987) indicate $\alpha = 18° \pm 2°$ in the flare region at a distance R from the nucleus of $R \geq 4''$ and $\alpha \leq 4°$ at $R \leq 3''$. This implies a mean density contrast of

$$\langle \rho_0(R \leq 3'') \rangle / \langle \rho_0(R \geq 4'') \rangle \geq 20 . \quad (5)$$

Using a volume filling factor of molecular gas of $f < 10^{-3}$ (Rotaciuc et al. 1991), we obtain a density contrast between atomic medium and circumnuclear molecular clouds of more than 2×10^4, in good agreement with the observed values and hence consistent with our proposal that the jet emerges from the dense molecular disk and enters lower density atomic gas. Wilson & Ulvestad's (1987) bow shock model with $\langle n_0 \rangle = 1$ cm^{-3} seems therefore appropriate for describing bow shock and jet. In this case Wilson & Ulvestad (1987) derive shock velocities of $v_0 \sim 500$–800 km s^{-1} in the bow shock region. Assuming a mean density of about $n_s \sim 50$ cm^{-3} in the circumnuclear molecular clouds (Rotaciuc et al. 1991) and using the equation $v_s^2/v_0^2 = n_0/n_s$ (Spitzer 1978), the shock velocity in the [Fe II] emitting region should be $v_s \sim 70$–110 km s^{-1}, a value typical of J-shocks. It therefore seems plausible to attribute the observed [Fe II] emission at least partially to an interaction of nuclear outflow and circumnuclear molecular clouds (while another part would come from excitation by the hard nuclear radiation).

An alternative to our above proposed AGN-dominated scenario would be to invoke a stellar origin for the observed [Fe II] emission. Oliva & Moorwood (1990) have suggested that the cooling-postshock zones of SNR's could account for the bright nuclear [Fe II] emission in NGC 1068. In fact, a SNR origin of the [Fe II] is, at least energetically, probably consistent with our observations: If we assume that $\sim 0.2\%$ of the total supernova kinetic energy ($\sim 10^{51}$ ergs) is converted into [Fe II] 1.64 μm emission, a value consistent with the observed ratio of [Fe II] luminosity to total luminosity in the SNR RCW 103 (Oliva et al. 1989), the supernova rate *required* to account for the observed [Fe II] flux within ~ 50 pc of the nucleus and of the flare peak, is 0.11 and 0.06 yr^{-1}, respectively. Using the relationship between supernova rate ν_{SN} and total 6 cm radio flux $S_{6\,cm}$ (Rotaciuc et al. 1991) $\nu_{SN} = 8.6 \times 10^{-3} S_{6\,cm}(\mathrm{Jy}) d^2(\mathrm{Mpc})$ with $d = 14$ Mpc, the *expected* 6 cm radio fluxes are ~ 60 mJy (nucleus) and ~ 30 mJy (flare). This is smaller than the 6 cm radio fluxes measured by Wilson & Ulvestad (1987): 320 mJy (nucleus) and 55 mJy (flare). Taking into account that the aforementioned conversion efficiency of total SN kinetic energy into [Fe II] 1.64 μm line flux is only a rough estimate, we conclude that the measured radio continuum and [Fe II] line fluxes are probably consistent with a SNR origin.

Although our observations cannot currently *exclude* a SNR origin for the [Fe II] emission, the observed morphology of the [Fe II], H_2, radio, and optical emission strongly suggests that the [Fe II] emission is produced in the interaction of nuclear outflow/radiation and circumnuclear molecular clouds, supporting our AGN-dominated scenario.

4. CONCLUSIONS

Our near-infrared imaging spectroscopy of the nucleus of NGC 1068 suggests that the [Fe II], H_2, radio continuum, and optical line emission observed toward the NLR arises at the interface between the nuclear outflow/radiation and circumnuclear molecular clouds. The [Fe II] emission also originates in the dense [$n(H_2) > 10^4$ cm^{-3}] outflow/cloud interfaces and may be produced in gas exposed to nuclear X-ray radiation or in gas which is interacting with the outflow/jet from the active nucleus. The abundance of iron appears to be enhanced along the jet axis. We propose that this enhancement may be due to efficient grain destruction by the hard nuclear radiation or fast J-shocks produced in the outflow and/or due to an unusually high value of the total fractional abundance of iron compared to solar. When leaving the molecular disk, the outflow/jet enters less dense atomic gas at a much lower pressure which causes the jet to widen. This flaring is seen both in the [Fe II] and radio emission. Alternatively, but less likely, the [Fe II] emission may be emitted in gas shocked by supernova remnants.

Our results also provide further insight into a possible origin of the large obscuration of the nucleus as inferred from optical polarization measurements: The high signal-to-noise quality of the new H_2 data have enabled us to ascertain that the warm molecular gas is not symmetrically distributed about the near-infrared continuum peak as was previously suspected. In contrast, the brightest H_2 line emission knot is centered within 0.″3 (20 pc) of the near-infrared continuum peak. It has a column density in excess of 10^{23} cm^{-2}, corresponding to $A_V > 50^m$, and probably represents molecular clouds near and along the line of sight to the nucleus.

We thank the staff of the William Herschel Telescope, especially H. Slingerland, for their excellent support during the observations. We would also like to thank V. Rotaciuc and G. Sämann for their work on the MPE FAST instrument and A. Eckart for making available his implementation of the Lucy-Richardson algorithm. Finally we are grateful to D. Forbes for his assistance with the observations. The William Herschel Telescope is operated on the island of La Palma by the Royal Greenwich Observatory in the Spanish Observatorio del Roque de los Muchachos of the Instituto de Astrofisica de Canarias.

REFERENCES

Antonucci, R. R. J., & Miller, J. S. 1985, ApJ, 297, 621
Bally, J., Stark, A. A., Wilson, R. W., & Henkel, C. 1988, ApJ, 324, 223
Cameron, M., Storey, J. W. V., Rotaciuc, V., Genzel, R., Verstraete, L., Drapatz, S., Siebenmorgen, R., & Lee, T. J. 1993, ApJ, 419, 136
Cecil, G., Bland, J., & Tully, R. B. 1990, ApJ, 355, 70
DePoy, D. L. 1992, ApJ, 398, 512
Evans, I. N., Ford, H. C., Kinney, A. L., Antonucci, R. R. J., Armus, L., & Caganoff, S. 1991, ApJ, 369, L27
Gallais, P. 1991, Ph.D. thesis (Paris: Univ. of Paris)
Graham, J. R., Wright, G. S., & Longmore, A. J. 1987, ApJ, 313, 847
Greenhouse, M. A., Woodward, C. E., Thronson, H. A., Jr., Rudy, R. J., Rossano, G. S., Erwin, P., & Puetter, R. C. 1991, ApJ, 383, 164
Halpern, J. P., & Grindlay, J. E. 1980, ApJ, 242, 1041
Halpern, J. P., & Oke, J. B. 1986, ApJ, 301, 753
Johansson, S. 1978, Phys. Scripta, 18, 217
Koski, A. T. 1978, 223, 56
Laor, A., & Draine, B. T. 1993, ApJ, 402, 441
Lowe, R. P., Moorhead, J. M., & Wehlau, W. H. 1979, ApJ, 228, 191
Lucy, L. B. 1974, AJ, 79, 745
Lynds, R. 1991, ApJ, 369, L31
Marshall, F. E., et al. 1993, ApJ, 405, 168
Miller, J. S., Goodrich, R. W., & Mathews, W. G. 1991, ApJ, 378, 47
Morton, D. C. 1991, ApJS, 77, 119
Mouri, H., Kawara, K., & Taniguchi, Y. 1993, ApJ, 406, 52
Nussbaumer, H., & Storey, P. J. 1980, A&A, 193, 327
———. 1988, A&A, 89, 308
Oliva, E., & Moorwood, A. F. M. 1990, ApJ, 348, L5
Oliva, E., Moorwood, A. F. M., & Danziger, I. J. 1989, A&A, 214, 307
Osterbrock, D. E. 1989, Astrophysics of Gaseous Nebulae and Active Galactic Nuclei (Mill Valley, CA: University Science Books)
Planesas, P., Scoville, N., & Myers, S. T. 1991, ApJ, 369, 364
Pogge, R. W. 1988, ApJ, 328, 519
Pradhan, A. K., & Zhang, H. L. 1993, ApJ, 409, L77
Rotaciuc, V. 1992, Ph.D. thesis, Ludwig Maximilian University (Munich)
Rotaciuc, V., Krabbe, A., Cameron, M., Drapatz, S., Genzel, R., Sternberg, A., & Storey, J. W. V. 1991, ApJ, 370, L23
Savage, B. D., & Mathis, J. S. 1979, ARA&R, 17, 73
Schultz, G. V., & Wiemer, W. 1975, A&A, 43, 133
Scoville, N. Z., Matthews, K., Carico, D. P., & Sanders, D. B. 1988, ApJ, 327, L61
Seab, C. G., & Shull, J. M. 1983, ApJ, 275, 652
Shull, J. M., & Draine, B. T. 1987, in Interstellar Processes, ed. D. J. Hollenbach & H. A. Thronson (Dordrecht: Reidel), 283
Shull, J. M., & McKee, C. F. 1979, ApJ, 227, 131
Snijders, M. A. J., Netzer, H., & Boksenberg, A. 1986, MNRAS, 222, 549
Spitzer, L. 1978, Physical Processes in the Interstellar Medium (New York: Wiley)
Steenberg, M. E., & Shull, J. M. 1988, ApJ, 330, 942
Sternberg, A., & Dalgarno, A. 1989, ApJ, 338, 197
Thronson, H. A. Jr., et al. 1989, ApJ, 343, 158
Ulvestad, J. S., Neff, S. G., & Wilson, A. S. 1987, AJ, 93, 22
Walker, M. F. 1968, ApJ, 151, 71
Ward, M. J., Geballe, T., Smith, M., Wade, R., & Williams, P. 1987, ApJ, 316, 138
Wills, B. J., Netzer, H., & Wills, D. 1985, ApJ, 288, 94
Wilson, A. S., & Ulvestad, J. S. 1983, ApJ, 275, 8
———. 1987, ApJ, 319, 105